光学学报

X射线偏振探测器中的极化光电过程模拟

郑人洲，强鹏飞*，盛立志**，闫永清
中国科学院西安光学精密机械研究所瞬态光学与光子技术国家重点实验室，陕西 西安 710119

摘要 采用蒙特卡罗程序Geant4模拟2～10 keV线偏振X射线光子在几种常用工作气体中的极化光电过程，明确了光电子出射位置、方位角分布与入射光子偏振方向、能量之间的响应关系。光电子的出射方向在入射光子偏振方向上的分布概率最高，且出射光电子的方位角分布可近似为余弦平方函数。光子能量增大时，各角度光电子计数不同程度地减少，但都呈现出在方位角为0或π(－π)时有极大值的统计规律。此外，揭示并量化了气体厚度、气体组成、气体体积分数之比和光子能量对探测效率的影响规律。气体厚度越大、平均原子序数越大，则探测效率越高。光子能量增大会导致探测效率降低，而对于由Xe或Ar组成的工作气体，当光子能量大于某壳层电子结合能时，由于相应壳层电子开始被弹射出，探测效率会有一定程度的提高。这些结果可为X射线偏振探测器的结构设计提供理论依据和数据支持。

关键词 X射线光学；X射线偏振探测；气体探测器；极化光电过程；探测效率

中图分类号 TL816＋.1 **文献标志码** A **DOI：** 10.3788/AOS231631

1 引　　言

X射线偏振探测是研究黑洞、脉冲星等强X射线源天体物理性质及相关伽马射线暴等天文现象的重要手段，可以提供天体的磁场分布信息，有助于了解相关的物理过程和辐射机制。通过偏振探测可以揭示黑洞的形成过程和相对论喷流的产生机制，可以推断脉冲星风云的几何形状和周围介质特性，也可以明晰伽马射线暴的爆发机制[1-3]。X射线偏振探测是突破光谱、时变和成像这三个维度天体物理信息来源的第四维信息窗口。

早期的X射线偏振探测器主要是汤姆孙散射偏振计和布拉格偏振计，但由于调制因子小、探测能段窄等原因没有得到较理想的偏振测量结果[4-5]。2001年，Costa等[6]提出了一种利用光电效应进行X射线偏振探测的新方式，即通过气体探测器对X射线光子产生的光电子径迹进行成像来获得X射线的偏振信息，自此X射线偏振探测研究才真正开始。近年来，多个搭载X射线偏振探测器的空间科学卫星已经或计划发射升空。2018年，由清华大学等多家单位合作完成的软X射线偏振探测器PolarLight搭载在立方体卫星上发射升空，用于观测Crab Nebula等X射线源，探测能段为2～8 keV[7]。2021年，入选美国国家航空航天局天体物理小型探测卫星计划的成像X射线偏振探测器(IXPE)发射升空，用于观测黑洞、中子星、超新星残余等明亮X射线源的偏振，探测能段为2～8 keV[8]。增强型X射线时变与偏振卫星(eXTP)是在我国研制X射线时变与偏振卫星项目基础上提出的大型X射线天文卫星项目，计划2025年发射升空，观测目标是处于极端物理条件下的黑洞、中子星等，探测能段可拓宽至0.5～30 keV[9]。

极化光电过程是探测器能够实现偏振探测的关键物理过程，明确其中的光子-气体相互作用过程和出射光电子分布规律对于深入理解探测器的工作机制具有重要意义，同时也能为探测器的结构设计提供参考。因此，极化光电过程是X射线偏振探测和偏振探测器研制过程中的重要研究内容，已有很多相关的研究被报道[10-17]。2013年，Wang等[18]利用Geant4程序模拟了气体中的光电吸收过程，并计算了Ne和CO_2混合气体在2～10 keV能段下的调制因子。2021年，Huang等[19]利用Geant4和Garfield＋＋程序对探测效率和光电子径迹产生进行模拟，分析了X射线能量对Ne和二甲醚(DME)混合气体探测效率的影响。2022年，Zhang等[20]对基于Xe的气体探测器进行了仿真研究，验证了其对10～30 keV X射线的偏振探测能力。可以看到，多种混合气体被用于气体探测器的X射线偏振探测，这些模拟结果重现了X射线偏振探测器中的重要物理过程，便于去分析探测器性能的主要影响因

收稿日期： 2023-10-09；**修回日期：** 2023-11-06；**录用日期：** 2023-11-13；**网络首发日期：** 2023-11-23

基金项目： 国家自然科学基金(42327802，62271483)、国家重点实验室基金(SKLIPR2021)、陕西省自然科学基础研究计划重点项目(2023-JC-ZD-40)

通信作者： *qiangpengfei@opt.ac.cn；**lizhi_sheng@opt.ac.cn

素。同时也可以注意到，不同种类气体的性质不同，这会影响极化光电过程中的粒子输运，进一步导致不同的探测效果，因此有必要通过模拟对不同条件下的极化光电过程进行研究，这能为针对不同探测目标选择合适的混合气体种类和比例提供参考。

本文采用蒙特卡罗程序Geant4模拟2～10 keV线偏振X射线光子在几种常用工作气体中的极化光电过程，讨论光电子出射位置、方位角分布与入射光子偏振方向、能量之间的响应关系，最后分析气体厚度、气体组成、气体体积分数之比和光子能量对探测效率的影响，这些结果可为X射线偏振探测器的结构设计提供理论依据和数据支持。

2　X射线偏振探测器原理

X射线与物质相互作用时，主要发生三种相互作用：光电效应、康普顿效应和电子对效应。X射线偏振探测器则是利用光电效应过程中光电子出射方向受入射光子偏振矢量调制进行偏振测量的。在进行X射线偏振测量时，通常使用气体探测器获得光电子的径迹图像，进一步从光电子径迹的前半段通过径迹重建算法拟合出光电子的出射方向，最后通过统计光电子出射方向的方位角分布便可得到X射线的偏振信息。

图1所示为光子与物质发生光电效应时产生光电子的示意图，光电子出射方向与光子入射方向的夹角为θ，光电子在XY平面上的投影矢量与X轴的夹角为φ。在非相对论近似条件下，入射光子与物质发生光电效应的K层光电截面(σ)[21]满足

$$\frac{\mathrm{d}\sigma}{\mathrm{d}\Omega}=r_0^2 Z^5\alpha^4\left(\frac{m_e c^2}{h\nu}\right)^{7/2}\frac{4\sqrt{2}\,\sin^2\theta\cos^2\varphi}{\left(1-\beta\cos\theta\right)^4},\qquad(1)$$

式中：Ω为立体角；r_0为电子经典半径；Z为物质的原子序数；β为光电子速度；α为精细结构常数，表示电子在第一玻尔轨道上的运动速度和真空中光速的比值，一般取值为1/137。对于低能光子，光电截面与$\sin^2\theta\cos^2\varphi$成正比，在$XY$平面上，光电截面则与$\cos^2\varphi$成正比。

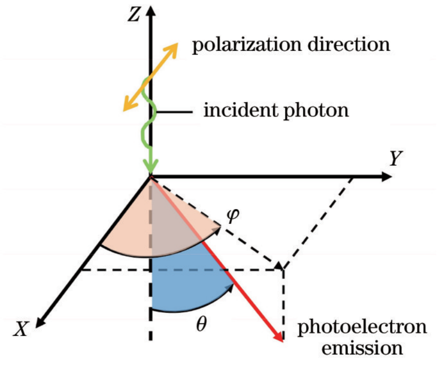

图1　光子与物质发生光电效应产生光电子的示意图

Fig. 1　Schematic diagram of photoelectrons produced by photoelectric effect between photons and matter

3　极化光电过程模拟

气体探测器中的工作气体通常为稀有气体（He、Ne、Ar等）和C或H的多原子化合物（CH_4、CO_2、CF_4等）组成的混合气体，工作气体的平均原子序数、密度等都会影响X射线光子的极化光电过程。表1所示为常温、常压条件下常用气体的物理性质[22-23]，表中Z_{atom}为原子序数，A为质量数，ρ为密度，E_X为第一激发能，E_I为电离能，W_I为平均电离能。

表1　常温、常压条件下常用气体的物理性质[22-23]

Table 1　Physical properties of commonly used gases under normal temperature and pressure conditions[22-23]

Gas	Z_{atom}	A	ρ /(mg/cm^3)	E_X /eV	E_I /eV	W_I /eV
He	2	2	0.179	19.8	24.6	41
Ne	10	20	0.839	16.7	21.6	37
Ar	18	40	1.66	11.6	15.7	26
Xe	54	131	5.495	8.4	12.1	22
CH_4	10	16	0.667	8.8	12.6	30
C_4H_{10}	34	58	2.49	6.5	10.6	26
CO_2	22	44	1.84	7.0	13.8	34
CF_4	42	88	3.78	10.0	16.0	54
DME	26	46	2.20	6.4	10.0	24

本文采用蒙特卡罗程序Geant4模拟2～10 keV线偏振X射线光子在常用工作气体中的极化光电过程，模拟模型如图2(a)所示，气体室尺寸为2 cm×2 cm×H，H为气体厚度，取值范围为0.1～10 cm，光子沿Z轴方向入射，选择的工作气体组合包括：He+C_3H_8、Ne+CF_4、Ne+DME、Ar+CH_4、Ar+CO_2、Xe+CO_2、CF_4+C_4H_{10}和DME+CO_2。选用G4EmLivermorePolarizedPhysics这一物理过程，根据光电反应截面计算发生概率，根据微分截面计算光电子出射的立体角分布，即可实现对极化光电过程的模拟。图2(b)～(d)所示为2 keV光子射入1 cm厚90%Ne+10%DME混合气体（90%和10%都指体积分数，下同）时粒子径迹的模拟结果（隐藏工作气体几何模型）。为更清晰地反映光电子的径迹和分布，模拟的event数量为10^3，通过逐渐放大视图可以观察到X射线的入射方向和光电子径迹。

在Geant4中，粒子与材料的相互作用过程按照相互作用节点被分割和记录，每一个“step”表示粒子与材料发生一次相互作用。图3所示为采用PreStepPoint提取到的2 keV光子射入1 cm厚90%Ne+10%DME混合气体时每个光电子第一个“step”的位置信息在XY平面上的投影，光电效应产生的光电子出射后，会与气体原子不断发生碰撞，经过多次散射损失完所有动能后最终停下来，仅初始阶段的径迹包含有效的出射方向信息，因此仅第一个“step”作用位置信息可以反映光电子的出射方向。图3(a)

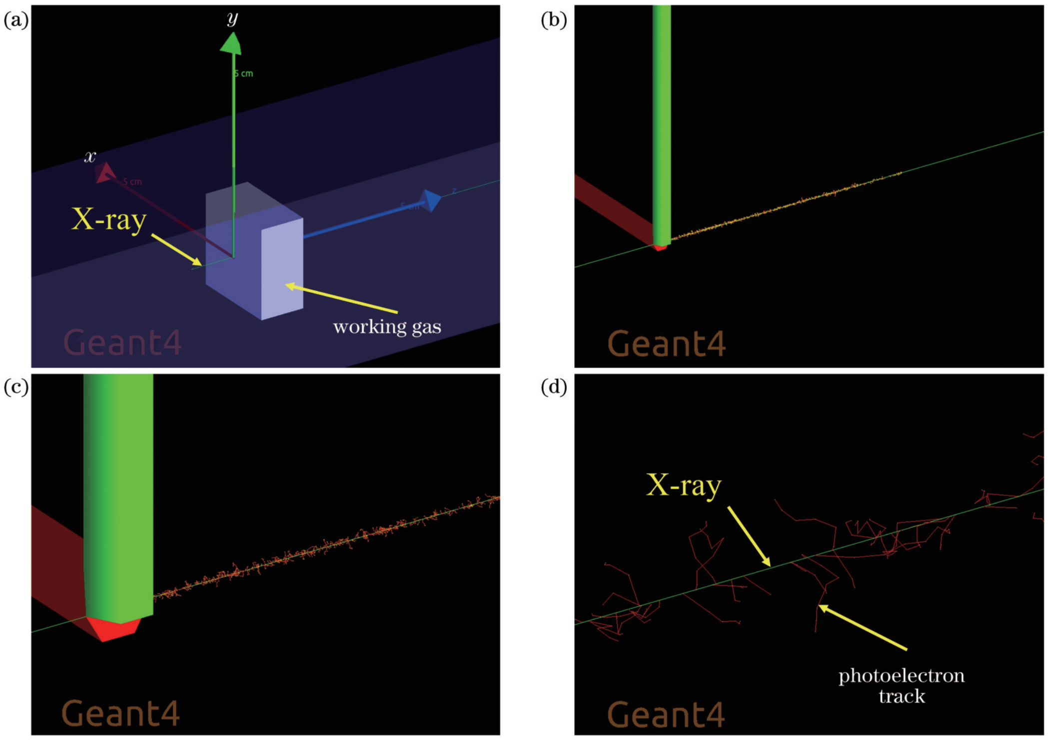

图2　极化光电过程Geant4模拟模型和2 keV光子射入1 cm厚90%Ne+10%DME混合气体时粒子径迹模拟结果。（a）极化光电过程Geant4模拟模型；（b）模拟结果视图1；（c）模拟结果视图2；（d）模拟结果视图3

Fig. 2　Geant4 simulation model of polarimetric photoelectric process, and particle track simulation results for 2 keV photons entering into 1 cm-thick 90%Ne+10%DME gas mixture. (a) Geant4 simulation model of polarimetric photoelectric process; (b) view 1 of simulation results; (c) view 2 of simulation results; (d) view 3 of simulation results

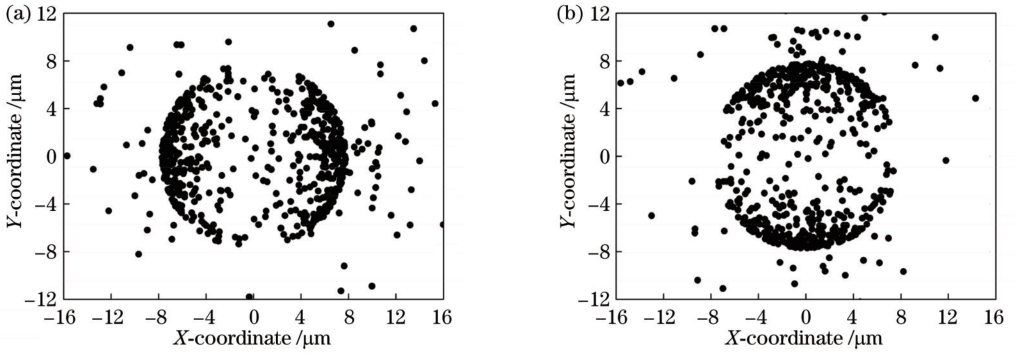

图3　2 keV光子射入1 cm厚90%Ne+10%DME混合气体时每个光电子第一个“step”的位置信息在XY平面上的投影。（a）入射光子偏振方向沿X轴方向；（b）入射光子偏振方向沿Y轴方向

Fig. 3　Projection of position information of the first "step" of each photoelectron on XY plane for 2 keV photons entering into 1 cm-thick 90%Ne+10%DME gas mixture. (a) Incident photon polarization direction is along X-axis; (b) incident photon polarization direction is along Y-axis

和（b）中分别定义入射光子的偏振方向为沿X轴方向和沿Y轴方向，可以看到，光电子的出射方向在入射光子偏振方向上的分布概率最高。

图4（a）～（d）所示为不同能量光子射入1 cm厚90%Ne+10%DME混合气体时每个光电子第一个“step”的位置信息在XY平面上的投影（入射光子偏振方向沿X轴方向），随着光子能量的增大，发生光电效应的反应截面减小，一定体积气体（1 cm厚）内产生的光电子数目减少，探测效率降低。图5所示为2 keV光子射入1 cm厚90%Ne+10%DME混合气体时若干光电子径迹在XY平面上的投影，在初始阶段的径迹上标示出了有效的出射方向。

图6统计了不同能量光子入射时出射光电子的φ分布（入射光子偏振方向沿X轴方向，模拟的event数量为10^4），可近似为余弦平方函数并用$n=A+B\cos^2(\varphi-\varphi_0)$进行拟合，式中$n$为计数，拟合参数$A$、$B$和$\varphi_0$分别表示非极化分量、极化分量和偏振方向位角。光子能量增大时，各角度光电子计数不同程度地减少，

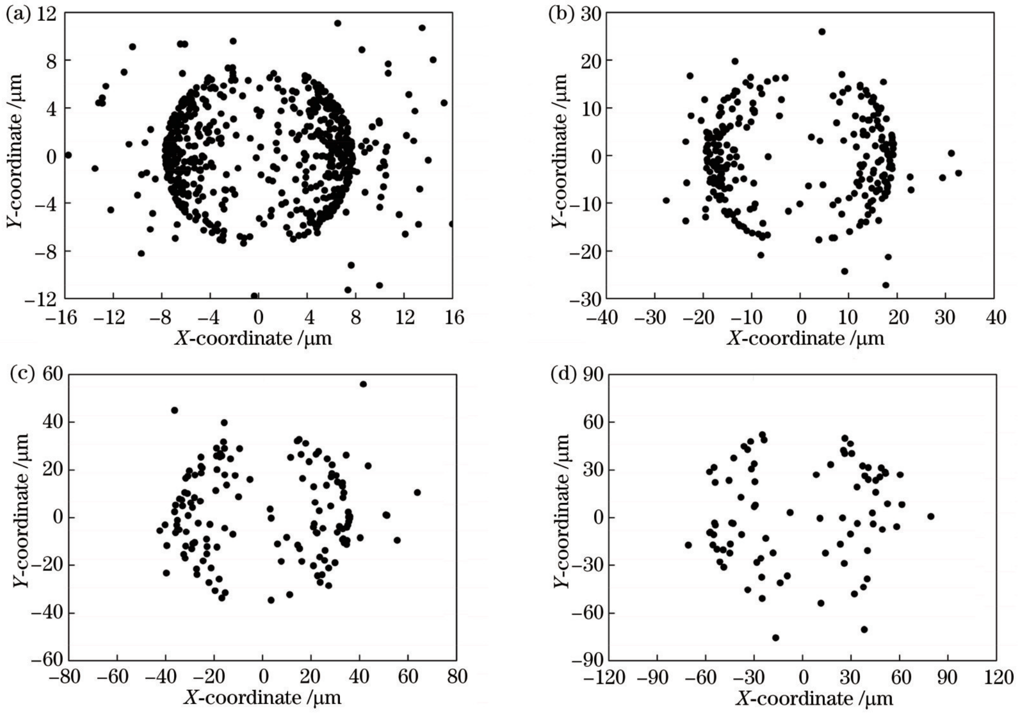

图4　不同能量光子射入1 cm厚90%Ne+10%DME混合气体时每个光电子第一个“step”的位置信息在XY平面上的投影（入射光子偏振方向沿X轴方向）。(a)2 keV；(b)3 keV；(c)4 keV；(d)5 keV

Fig. 4　Projection of position information of the first "step" of each photoelectron on XY plane for photons with different energies entering into 1 cm-thick 90%Ne+10%DME gas mixture (incident photon polarization direction is along X-axis). (a) 2 keV; (b) 3 keV; (c) 4 keV; (d) 5 keV

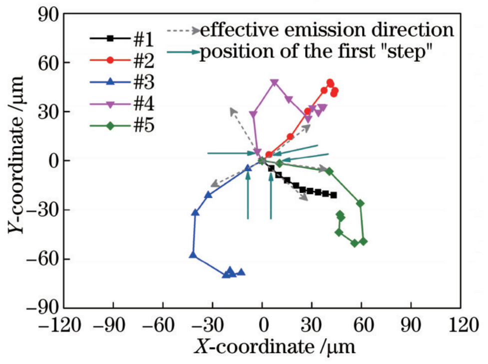

图5　2 keV光子射入1 cm厚90%Ne+10%DME混合气体时若干光电子径迹在XY平面上的投影

Fig. 5　Projection of several photoelectron tracks on XY plane for 2 keV photons entering into 1 cm-thick 90%Ne+10%DME gas mixture

但都呈现出在φ为0或π（$-\pi$）时有极大值的统计规律。

4　探测效率影响因素分析

探测效率是X射线偏振探测器选择工作气体时的重要标准，它是指X射线进入探测器发生光电效应并被探测器收集到的event数与X射线总光子数的比值，一般受气体体积、气体组成、气体体积分数之比、光子能量等的影响。图7所示为2 keV光子射入90%Ne+10%DME混合气体时气体厚度对探测效率的影响。为提高模拟结果的准确性，模拟的event数量增加至10^5。当气体厚度较小时，随着气体厚度的增加，探测效率迅速提升，从0.1 cm时的不足0.1提升到1 cm时的0.64；当气体厚度增加到3 cm时，探测效率大于0.9；之后随着气体厚度的增加，探测效率逐渐趋近于1。

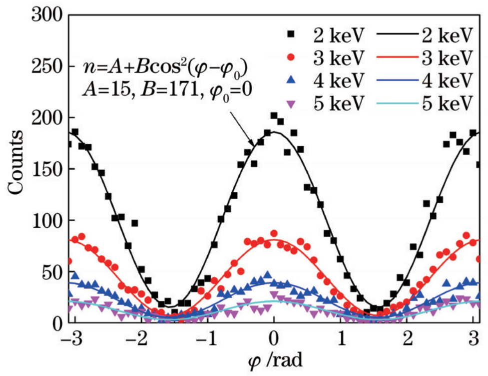

图6　不同能量光子入射时出射光电子的φ分布（入射光子偏振方向沿X轴方向，模拟的event数量为10^4）

Fig. 6　φ distribution of emission photoelectrons for incident photons with different energies (incident photon polarization direction is along X-axis, and number of events in simulation is 10^4)

图8所示为光子射入1 cm厚不同混合气体（气体体积分数之比均为90∶10，即90%+10%）时光子能量

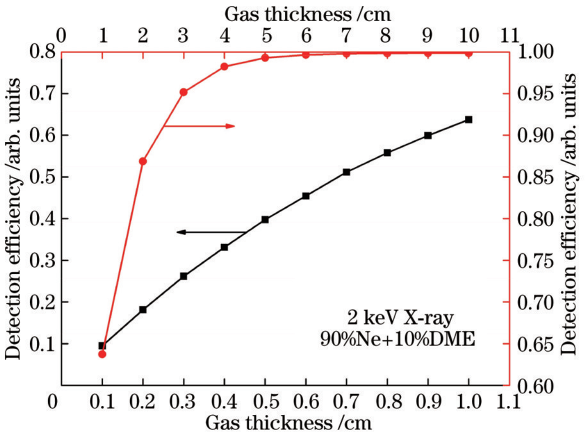

图 7　2 keV 光子射入 90%Ne+10%DME 混合气体时气体厚度对探测效率的影响

Fig. 7　Effect of gas thickness on detection efficiency for 2 keV photons entering into 90%Ne+10%DME gas mixture

对探测效率的影响，对于 $CF_4+C_4H_{10}$、$Ne+CF_4$、Ne+DME、DME+CO_2和 He+C_3H_8，探测效率随光子能量的增大而降低，且气体平均原子序数越大，探测效率越高。对于 Xe+CO_2，当光子能量从 4 keV 增大到 5 keV 时，探测效率有小幅上升，这是因为 Xe 原子 L_3壳层的电子结合能 E_{binding}为 4.79 keV[24]，光子能量大于 E_{binding}时可弹射出 L_3壳层的电子。类似地，对于 Ar+CO_2和 Ar+CH_4，当光子能量从 3 keV 增大到 4 keV 时，探测效率也有一定程度的提高，这是因为 Ar 原子 K 壳层的电子结合能 E_{binding}为 3.21 keV[24]，光子能量大于 E_{binding}时可弹射出 K 壳层的电子。

图 9(a)～(h)所示为光子射入 1 cm 厚不同比例混合气体时光子能量对探测效率的影响，图 9(i)所示为 2 keV 光子射入 1 cm 厚不同混合气体时气体体积分数之比对探测效率的影响，混合气体 Ne+DME、Xe+CO_2中探测效率的计算结果与 Huang 等[19-20]等的模拟结果一致(不考虑铍窗)，表明本工作中的模拟结果是准确的。可以看到，除 Ar+CO_2受 K 壳层电子出射影响外，提高大原子序数气体体积分数能有效提高各能量段的探测效率。在本文选择的工作气体组合中，90%Xe+10%CO_2对 2 keV 光子的探测效率最高，90%He+10%C_3H_8对 2 keV 光子的探测效率最低，仅为 0.05，而增加 C_3H_8的体积分数至 90% 时，探测效率可提高 6 倍以上。

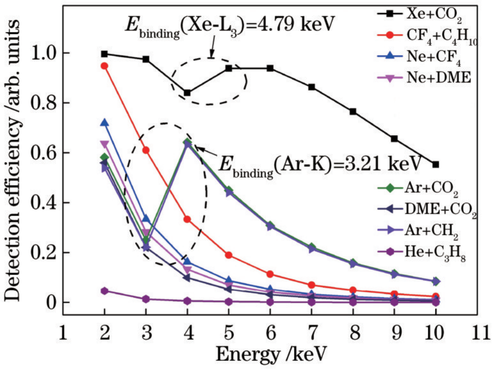

图 8　光子射入 1 cm 厚的不同混合气体时光子能量对探测效率的影响

Fig. 8　Effect of photon energy on detection efficiency for photons entering into different gas mixtures with thickness of 1 cm

需要指出的是，X 射线偏振探测器选择工作气体时一般从探测效率和光电子径迹两方面进行考虑，本文仅在探测效率方面进行了讨论，实际选择时还应结合气体中电子的漂移性质。考虑光电子漂移和扩散对其径迹粗细和长短的影响，以及径迹重建算法的重建效率等，根据光电子径迹进行 X 射线偏振测量时，细长的径迹有利于提取出光电子的出射方向，因此要减少电子的扩散，一般选择电子在其中扩散系数较小的工作气体，例如 DME、CF_4、CO_2等[25]。

5　结　　论

本文采用蒙特卡罗程序 Geant4 模拟了 2～10 keV 线偏振 X 射线光子在几种常用工作气体中的极化光电过程，明确了光电子出射位置、方位角分布与入射光子偏振方向、能量之间的响应关系。光电子的出射方向在入射光子偏振方向上的分布概率最高，且出射光电子的 φ 分布可近似为余弦平方函数。光子能量增大时，各角度光电子计数不同程度地减少，但都呈现出在方位角为 0 或 π(−π)时有极大值的统计规律。此外，揭示并量化了气体厚度、气体组成、气体体积分数之比和光子能量对探测效率的影响规律。气体厚度越大、平均原子序数越大，探测效率越高。光子能量增大会导致探测效率降低，而对于由 Xe 或 Ar 组成的工作气体，当光子能量大于某壳层电子结合能时，由于相应壳层电子开始被弹射出，探测效率会有一定程度的提高。本文工作为 X 射线偏振探测器的结构设计提供了一定的理论依据和数据支持，实际选择工作气体时还应结合气体中电子的漂移性质，考虑光电子漂移和扩散对其径迹粗细和长短的影响，以及径迹重建算法的重建效率等。

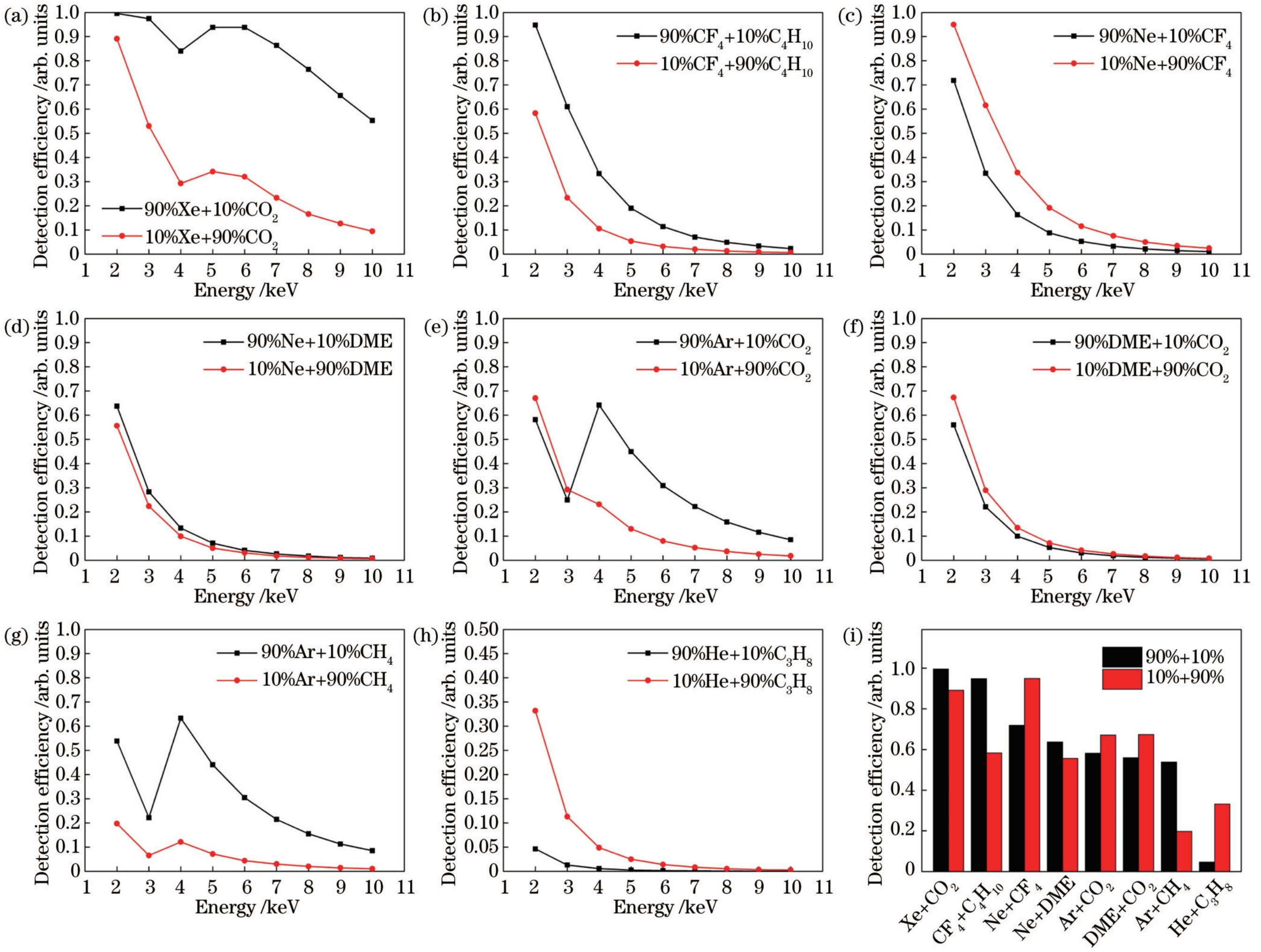

图 9　光子射入 1 cm 厚不同比例混合气体时光子能量对探测效率的影响。(a) Xe+CO_2；(b) CF_4+C_4H_{10}；(c) Ne+CF_4；(d) Ne+DME；(e) Ar+CO_2；(f) DME+CO_2；(g) Ar+CH_4；(h) He+C_3H_8；(i) 2 keV 光子射入 1 cm 厚不同混合气体时气体体积分数之比对探测效率的影响

Fig. 9　Effect of photon energy on detection efficiency for photons entering into 1 cm-thick gas mixtures with different ratios. (a) Xe+CO_2; (b) CF_4+C_4H_{10}; (c) Ne+CF_4; (d) Ne+DME; (e) Ar+CO_2; (f) DME+CO_2; (g) Ar+CH_4; (h) He+C_3H_8; (i) effect of gas volume fraction on detection efficiency for 2 keV photons entering into different gas mixtures with thickness of 1 cm

参考文献

[1] Rees M J. Expected polarization properties of binary X-ray sources[J]. Monthly Notices of the Royal Astronomical Society, 1975, 171(3): 457-465.

[2] Lundman C, Vurm I, Beloborodov A M. Polarization of gamma-ray bursts in the dissipative photosphere model[J]. The Astrophysical Journal Letters, 2018, 856(2): 145.

[3] 李岩松, 赵慧洁, 李娜, 等. 基于中红外偏振的海面太阳耀光背景下的目标探测[J]. 中国激光, 2022, 49(19): 1910004.
Li Y S, Zhao H J, Li N, et al. Detection of marine targets covered in Sun glint based on mid-infrared polarization[J]. Chinese Journal of Lasers, 2022, 49(19): 1910004.

[4] Weisskopf M C, Silver E H, Kestenbaum H L, et al. A precision measurement of the X-ray polarization of the Crab Nebula without pulsar contamination[J]. The Astrophysical Journal Letters, 1978, 220: L117-L121.

[5] Kestenbaum H L, Cohen G G, Long K S, et al. The graphite crystal X-ray spectrometer on OSO-8[J]. The Astrophysical Journal Letters, 1976, 210: 805-809.

[6] Costa E, Soffitta P, Bellazzini R, et al. An efficient photoelectric X-ray polarimeter for the study of black holes and neutron stars[J]. Nature, 2001, 411(6838): 662-665.

[7] Feng H, Bellazzini R. The X-ray polarimetry window reopens[J]. Nature Astronomy, 2020, 4(5): 547.

[8] Sgrò C. The imaging X-ray polarimetry explorer (IXPE)[J]. Nuclear Instruments and Methods in Physics Research Section A: Accelerators, Spectrometers, Detectors and Associated Equipment, 2019, 936: 212-215.

[9] Zhang S N, Santangelo A, Feroci M, et al. The enhanced X-ray Timing and Polarimetry mission: eXTP[J]. Science China Physics, Mechanics & Astronomy, 2019, 62(2): 29502.

[10] Kitaguchi T, Black K, Enoto T, et al. An optimized photoelectron track reconstruction method for photoelectric X-ray polarimeters[J]. Nuclear Instruments and Methods in Physics Research Section A: Accelerators, Spectrometers, Detectors and Associated Equipment, 2018, 880: 188-193.

[11] Depaola G O, Longo F. Measuring polarization in the X-ray range: new simulation method for gaseous detectors[J]. Nuclear Instruments and Methods in Physics Research Section A: Accelerators, Spectrometers, Detectors and Associated

Equipment, 2006, 566(2): 590-597.
[12] Strohmayer T E. X-ray spectro-polarimetry with photoelectric polarimeters[J]. The Astrophysical Journal Letters, 2017, 838 (1): 72.
[13] Markus G, Klaus D, Jochen K, et al. Development of a GridPix X-ray polarimeter[J]. Journal of Physics: Conference Series, 2022, 2374(1): 012148.
[14] Iwakiri W B, Black J K, Cole R, et al. Performance of the PRAXyS X-ray polarimeter[J]. Nuclear Instruments and Methods in Physics Research Section A: Accelerators, Spectrometers, Detectors and Associated Equipment, 2016, 838: 89-95.
[15] 石晶晶，胡亚东，李孟凡，等. 基于光谱调制的线偏振测量技术研究及精度验证[J]. 光学学报，2022，42(2): 0212003.
Shi J J, Hu Y D, Li M F, et al. Research and accuracy verification of linear polarization measurement technology based on spectral modulation[J]. Acta Optica Sinica, 2022, 42(2): 0212003.
[16] 高超，翁剑宇，曹晓昱，等. 空间调制型偏振检测技术研究现状及发展趋势[J]. 光学学报，2023，43(17): 1712004.
Gao C, Weng J Y, Cao X Y, et al. Research statues and prospects of spatially modulated polarimetry[J]. Acta Optica Sinica, 2023, 43(17): 1712004.
[17] 龚建伟，陈兵. 间接式X射线探测器的核心器件及其耦合方式[J]. 激光与光电子学进展，2022，59(7): 0700003.
Gong J W, Chen B. Core devices and coupling modes of indirect X-ray detectors[J]. Laser & Optoelectronics Progress, 2022, 59 (7): 0700003.
[18] Wang S, Ji J F, Han D, et al. Simulation of photoelectric X-ray polarimetry and reconstruction of the photoelectron azimuthal angle[J]. Chinese Physics C, 2013, 37(3): 036002.
[19] Huang X F, Liu H B, Zhang J, et al. Simulation and photoelectron track reconstruction of soft X-ray polarimeter[J]. Nuclear Science and Techniques, 2021, 32(7): 67.
[20] Zhang J, Cai X C, Huang Y B, et al. Simulation of a Xe-based X-ray polarimeter at 10-30 keV[J]. Journal of Instrumentation, 2022, 17(4): P04003.
[21] Bellazzini R, Brez A, Costa E, et al. Photoelectric X-ray polarimetry with gas pixel detectors[J]. Nuclear Instruments and Methods in Physics Research Section A: Accelerators, Spectrometers, Detectors and Associated Equipment, 2013, 720: 173-177.
[22] Sharma A. Properties of some gas mixtures used in tracking detectors[EB/OL]. [2023-06-05]. https://www.slac.stanford.edu/pubs/icfa/summer98/paper3/paper3.pdf.
[23] Workman R L, Burkert V D, Crede V, et al. Review of particle physics[J]. Progress of Theoretical and Experimental Physics, 2022, 2022(8): 083C01.
[24] Carlson T A. Photoelectron and auger spectroscopy[M]. New York: Plenum, 1976: 337-343.
[25] Li Z L, Feng H B, Huang X F, et al. Preliminary test of topmetal-II sensor for X-ray polarization measurements[J]. Nuclear Instruments and Methods in Physics Research Section A: Accelerators, Spectrometers, Detectors and Associated Equipment, 2021, 1008: 165430.

Simulation of Polarimetric Photoelectric Process in X-Ray Polarization Detector

Zheng Renzhou, Qiang Pengfei*, Sheng Lizhi**, Yan Yongqing
State Key Laboratory of Transient Optics and Photonics, Xi'an Institute of Optics and Precision Mechanics, Chinese Academy of Sciences, Xi'an 710119, *Shaanxi, China*

Abstract

Objective X-ray polarization detection is an important means to study the astrophysical properties of intense X-ray sources such as black holes, pulsars, and related gamma-ray bursts. The development of X-ray polarization detectors with excellent performance is the technical basis for related research. Early X-ray polarization detectors were mainly Thomson scattering polarimeters and Bragg polarimeters. However, due to the low modulation factor and narrow detection energy range, the ideal polarization measurement results were not obtained. In 2001, Costa *et al*. proposed a new way of X-ray polarization detection using the photoelectric effect, in which the X-ray polarization information was obtained by imaging the photoelectron track produced by X-ray photons through a gas detector. The polarimetric photoelectric process is the key physical process for the detector to realize polarization detection. It is of great significance to clarify the photon-gas interaction process and the distribution law of emitted photoelectrons for further understanding the working mechanism of the detector. The polarimetric photoelectric process is an important research content in the development of this type of X-ray polarization detector. Different types of gases have various properties, which will affect the particle transport in the polarimetric photoelectric process and further leads to different detection efficiencies. Therefore, it is necessary to simulate the polarimetric photoelectric process under different conditions. This can provide a theoretical basis and data support for the structure design of X-ray polarization detectors.

Methods We simulate the polarimetric photoelectric process of 2-10 keV linearly polarized X-ray photons in several commonly used working gases by the Monte Carlo code Geant4. The selected working gas combinations include He+C_3H_8, Ne+CF_4, Ne+DME, Ar+CH_4, Ar+CO_2, Xe+CO_2, CF_4+C_4H_{10}, and DME+CO_2. The response relationship of the emission position and azimuthal angle distribution of photoelectron with the polarization direction and energy of the incident photon is discussed. Moreover, the effects of gas thickness, gas component, gas ratio, and photon energy on the detection efficiency are analyzed.

Results and Discussions First, the response relationship of the emission position and azimuthal angle distribution of the photoelectron with the polarization direction and energy of the incident photon is clarified. The emission direction distribution probability of the photoelectron is the largest in the polarization direction of the incident photon, and the azimuthal angle distribution can be approximated as a cosine squared function. With the increase in photon energy, the counts of photoelectrons at each angle decrease in different degrees, but all of them show a statistical law that the maximum values occur when the azimuthal angle is 0 or π (−π) (Fig. 6). Moreover, the effects of gas thickness, gas component, gas ratio, and photon energy on the detection efficiency are revealed and quantified. For 2 keV photons entering into 90%Ne+10%DME gas mixture, when the gas thickness is small, the detection efficiency increases rapidly with the increase in gas thickness, from less than 0.1 at 0.1 cm to 0.64 at 1 cm (Fig. 7). When the gas thickness increases to 3 cm, the detection efficiency is greater than 0.9. Then, with the increase in gas thickness, the detection efficiency gradually approaches 1. For the $CF_4+C_4H_{10}$, $Ne+CF_4$, Ne+DME, $DME+CO_2$, and $He+C_3H_8$, the detection efficiency decreases with the increase in photon energy, and the large average atomic number of gas can lead to a high detection efficiency (Fig. 8). While for the $Xe+CO_2$, $Ar+CO_2$, and $Ar+CH_4$, when the photon energy is greater than the binding energy of certain shell electrons of Xe or Ar atoms, the detection efficiency will be improved to a certain extent because the corresponding shell electrons begin to be ejected. In addition to the $Ar+CO_2$ which is affected by the electron emission in K-shell, the detection efficiency in each energy range can be effectively improved by increasing the proportion of gas with high atomic number (Fig. 9).

Conclusions We simulate the polarimetric photoelectric process of 2‒10 keV linearly polarized X-ray photons in several commonly used working gases by the Monte Carlo code Geant4. The response relationship of the emission position and azimuthal angle distribution of the photoelectron with the polarization direction and energy of the incident photon is clarified. The emission direction distribution probability of the photoelectron is the largest on the polarization direction of the incident photon, and the azimuthal angle distribution can be approximated as a cosine squared function. With the increase in photon energy, the counts of photoelectrons at each angle decrease in different degrees, but all of them show a statistical law that the maximum values occur when the azimuthal angle is 0 or π (−π). Moreover, the effects of gas thickness, gas component, gas ratio, and photon energy on the detection efficiency are revealed and quantified. The larger gas thickness and larger average atomic number can lead to higher detection efficiency. In addition, the increase in photon energy can result in a decrease in detection efficiency. However, for the working gases composed of Xe or Ar, when the photon energy is greater than the binding energy of a certain shell electron, the detection efficiency will be improved to a certain extent because the corresponding shell electrons begin to be ejected. The results in this paper can provide some theoretical basis and data support for the structure design of X-ray polarization detectors. In the actual selection of working gases, the drift properties of electrons in gases, the effect of photoelectron drift and diffusion on track thickness and length, and the reconstruction efficiency of the track reconstruction algorithm should also be considered.

Key words X-ray optics; X-ray polarization detection; gas detector; polarimetric photoelectric process; detection efficiency